Rare Met. (2023) 42(2):438–448
https://doi.org/10.1007/s12598-022-02131-w

RARE METALS

ORIGINAL ARTICLE

Nitrogen-rich three-dimensional porous carbon mosaicked $Na_4Ge_9O_{20}$ as anode material for high-performance lithium-ion batteries

Hao-Miao Zhang, Jing Chen, Rou Lu, Cong-Ge Lu, Shuang Zhou, Zhi Chang*, An-Qiang Pan*

Received: 29 March 2022 / Revised: 28 April 2022 / Accepted: 9 May 2022 / Published online: 20 October 2022

Abstract Germanium-based material has attracted numerous attentions and been regarded as a promising anode material for lithium-ion batteries due to its high theoretical capacity. However, drastic pulverization and rapid capacity fading caused by large volume variation during cycling limit its practical application. In this work, three-dimensional N-doped carbon framework-wrapped $Na_4Ge_9O_{20}$ nanoparticles (3D $Na_4Ge_9O_{20}$@N-C) have been synthesized via freeze-drying approach with NaCl as both template and sodium source for ion-exchanging. The employment of NaCl has two special roles: on the one hand, the NaCl crystals act as template and facilitate the formation of 3D porous structure, while on the other hand, the NaCl crystals serving as sodium source and support the ion exchange between NaCl and GeO_2 promote the formation of $Na_4Ge_9O_{20}$. Benefiting from the unique method, the prepared 3D $Na_4Ge_9O_{20}$@N-C not only suppresses the volume change by using carbon as buffer layers but also demonstrates an improved electronic conductivity and a shortened ionic diffusion. When utilized as an anode material for LIBs, the 3D $Na_4Ge_9O_{20}$@N-C composites deliver high reversible capacity (896.2 $mAh{\cdot}g^{-1}$ at 0.1 $A{\cdot}g^{-1}$ after 100 cycles), good cycling stability (520.8 $mAh{\cdot}g^{-1}$ at 2.0 $A{\cdot}g^{-1}$after 400 cycles) and excellent rate performance (636.0 $mAh{\cdot}g^{-1}$ at 2.0 $A{\cdot}g^{-1}$). This work provides a strategy to improve the electrochemical performance of germanium-based anode materials for lithium-ion batteries.

Keywords Germanium-based anode; $Na_4Ge_9O_{20}$; N-doped carbon; Porous nanostructure; Lithium-ion batteries (LIBs)

1 Introduction

Over the past few years, lithium-ion batteries (LIBs) which possess high energy density, environmental benignity and long cycle life, are widely applied in various fields such as portable electronic devices and electric vehicles. Currently, graphite is used as commercial anode material due to its stable electrochemical performance and low cost. However, the low theoretical specific capacity (372 $mAh{\cdot}g^{-1}$) of graphite cannot meet the surging demands of energy storage applications. It is vital to develop advanced anode materials with higher capacity for LIBs [1, 2].

Recently, germanium (Ge) has been regarded as one of the promising anode materials to replace graphite in LIBs because of their intrinsic superiorities, such as high lithium-ion diffusivity (6.51×10^{-12} $cm^2{\cdot}s^{-1}$ at room temperature) [3], high theoretical capacity (1623 $mAh{\cdot}g^{-1}$) [4] and good surface stability [5]. Unfortunately, the destructive structural damage and exfoliation of active materials caused by the drastic volume expansion (more than 230%) during Li–Ge reactions of pure Ge anodes tend to result in rapid capacity fading. In addition, the high price

Supplementary Information The online version contains supplementary material available at https://doi.org/10.1007/s12598-022-02131-w.

H.-M. Zhang, R. Lu, C.-G. Lu, S. Zhou, Z. Chang*, A.-Q. Pan*
School of Materials Science and Engineering, Central South University, Changsha 410083, China
e-mail: zhichang@csu.edu.cn

A.-Q. Pan
e-mail: pananqiang@csu.edu.cn

J. Chen
School of Physics and Materials, Nanchang University, Nanchang 330031, China

of Ge-based materials greatly limits their practical applications [6]. An alternative method to overcome these obstacles is to synthesize binary or ternary germanium compounds, such as GeO_2 [7], GeS_2 [8], Zn_2GeO_4 [9], $Ca_2Ge_7O_{16}$ [10], and $CuGeO_3$ [11]. Compared with binary Ge compounds, the latter could decompose into corresponding metal oxides (e.g., CaO for $Ca_2Ge_7O_{16}$) which can serve as matrix buffers during the initial lithiation process and consequently adapt the volume change during initial cycling processes [12]. Meanwhile, metal oxides could enhance the electrical conductivity of the anode materials. For example, Li et al. [13] synthesized series of crystalline metal germanate nanowires, including $Ca_2Ge_7O_{16}$, $SrGe_4O_9$, and $BaGe_4O_9$ via simple hydrothermal method. These germanate nanowires, especially the $Ca_2Ge_7O_{16}$ nanowires, exhibited excellent electrochemical lithium storage properties. In addition, introducing other metallic elements into binary germanium materials and preparing ternary germanium compounds can effectively reduce the content of the expensive Ge, thus could reduce the expense of anode materials, which makes metal germinates stand out among various high-performance anodes. Owing to its natural abundance and relatively low price, Na is an element worth considering. Nevertheless, there are few reports about the application of $Na_4Ge_9O_{20}$.

The electrochemical performance of anode materials was greatly influenced by their morphology and microstructure [14]. To date, various strategies have been investigated intensively to improve the capacity as well as the cycling stability of anode materials by using carbon-based micro-structured designs, such as nanoflakes [15], nanowires [16], nanotubes [17], and porous structures [18]. Compositing the anode materials with carbon could improve the electronic conductivity and restrain the stress within the active materials [19]. Among these structures, three-dimensional (3D) porous structures have attracted increasing attention because of their large specific surface area/void space and short ionic and electronic transport pathway. This makes it possible to alleviate the huge volume variation and aggregation of the nanoparticles during the lithiation, thus consequently effectively increasing their cycling stability [20]. For instance, fabricated by Ngo et al. [21] and Ren et al. [22] via carbothermal reduction, the 3D porous Ge-C composite exhibits superior reversible capacity (1122 $mAh{\cdot}g^{-1}$ at 100C and 429 $mAh{\cdot}g^{-1}$ even at 400C) and cycling stability (over 1000 $mAh{\cdot}g^{-1}$ at 5 $A{\cdot}g^{-1}$ after 1200 continuous cycles). The ultrahigh rate performance of the composites is due to its porous 3D nanostructure. Besides, N-doping was frequently reported on improving the electronic conductivity of carbon by producing multiple defects and more active sites, and providing more storage for lithium ions [23, 24]. Therefore, we envisioned that it is essential to design a 3D porous ternary Ge compounds anode materials for lithium-ion batteries.

Herein, we report for the first time the synthesis of 3D porous $Na_4Ge_9O_{20}$@N-doped carbon composites by freeze-drying approach using NaCl as both template and sodium source for ion-exchanging. The prepared $Na_4Ge_9O_{20}$ nanoparticles are uniformly encapsulated inside the porous 3D carbon framework. The porous interconnected carbon structure could not only provide more valid pathway for electrons and lithium-ions, but also relieve the volume change of anode material upon the discharge/charge process [25]. More importantly, when utilized as anode for LIBs, 3D porous $Na_4Ge_9O_{20}$@N-doped carbon electrodes exhibit superior electrochemical performances in terms of high capacity, good rate capability and excellent cycling stability.

2 Experimental

2.1 Synthesis of materials

All chemicals were used as received without further purification. 0.05 g GeO_2 was dissolved in 25 ml deionized water, followed by adding 0.5 ml $NH_3{\cdot}H_2O$ to form a clear and transparent solution under stirring. 0.5 g polyvinyl pyrrolidone (PVP) was dissolved in another 10 ml deionized water. The above two solutions were mixed and stirred for 10 min. Then, 1.44 g NaCl was added and stirred for further 1 h at room temperature. The resulting solution was freeze-dried in a vacuum to produce the precursor. Afterward, the obtained precursor was carbonized in a tube furnace under Ar atmosphere at 600 °C for 5 h with a heating rate of 3 $°C{\cdot}min^{-1}$. To form the 3D porous $Na_4Ge_9O_{20}$@N-doped carbon (3D $Na_4Ge_9O_{20}$@N-C), the products were washed in deionized water to dissolve NaCl. Similarly, different amounts of GeO_2 (0.02 and 0.10 g) were used during the synthesis process and the obtained products were designated as 3D $Na_4Ge_9O_{20}$@N-C-L and 3D $Na_4Ge_9O_{20}$@N-C-H, respectively. For comparison, bare $Na_4Ge_9O_{20}$ and 3D N-C were prepared by the similar approach without the addition of PVP and GeO_2, respectively. The $Na_4Ge_9O_{20}$@N-C sample without porous structure was fabricated by evaporating the above-mentioned precursor solution instead of freeze drying, with a subsequent annealing treatment like that of 3D $Na_4Ge_9O_{20}$@N-C.

2.2 Structural characterization

The microscopic morphologies and elemental distribution of as-prepared products were observed by field-emission scanning electron microscope (FESEM, FEI Nova

NanoSEM 230) and transmission electron microscope (TEM, Titan G2 60–300), equipped with an energy-dispersive spectrometer (EDS). X-ray diffraction (XRD, Rigaku D/max 2500) was used to detect the crystalline structures of the composites. The chemical states and chemical bonds of each element on the surface were studied using X-ray photoelectron spectroscopy (XPS). The multi-point Brunauer–Emmett–Teller (BET) method was employed to calculate specific surface areas. Raman spectrometer analysis (LabRAM HR800) and thermogravimetric analysis (TGA, NETZSCH STA 499C) were conducted to investigate the graphitization degree and the content of carbon, respectively.

2.3 Electrode fabrication and electrochemical measurement

Electrochemical performances were measured by assembling 2016-type coin cell with lithium metal serving as the counter electrode in a recirculating ultrahigh-purity argon glove box (Mbraun, Germany). The working electrodes were prepared by coating a homogeneous viscous slurry containing 70% active materials, 20% super P, 10% sodium carboxymethyl cellulose (CMC) on the current collector (copper foil) before being dried under vacuum at 80 °C for 12 h. The electrodes were cut into 12-mm-diameter round pieces and the mass loading of the active material is between 0.8 and 1.0 mg. 1 mol·L^{-1} $LiPF_6$ in ethyl carbonate (EC)/dimethyl carbonate (DMC)/ethyl methyl carbonate (EMC) with a volume ratio of 1:1:1 was chosen as electrolyte, while polypropylene membrane was chosen as the separator.

The galvanostatic charge/discharge performances of the electrodes were carried out on a Land battery tester (Land CT2001A, Wuhan, China) in a voltage window of 0.01–3.00 V (vs. Li/Li^+). Cyclic voltammetry (CV, 0.01–3.00 V) curves were obtained from an electrochemical workstation (CHI660C, Shanghai, China) at a scan rate of 0.1 mV·S^{-1}. Electrochemical impedance spectrometry (EIS, from 100 kHz to 10 MHz) data were recorded on a ZAHNER-IM6ex electrochemical workstation (ZAHNER Co., Germany). All electrochemical measurements were performed at room temperature.

3 Results and discussion

3.1 Formation mechanism and structure characterization of materials

The fabrication process of the 3D porous $Na_4Ge_9O_{20}$@N-doped carbon (3D $Na_4Ge_9O_{20}$@N-C) composites is shown in Scheme 1. GeO_2 was used as Ge source, polyvinyl pyrrolidone (PVP) was used as both C and N source, NaCl was used as both Na source and assisted-template to construct the 3D porous carbon network. First, GeO_2 reacted with $NH_3{\cdot}H_2O$ in aqueous solution to form $(NH_4)_2GeO_3$ solution, followed by mixing with PVP and NaCl to form the precursor solution. During the process of freezing, the recrystallized NaCl cubes uniformly coated with $(NH_4)_2GeO_3$·PVP film were self-assembled into a 3D structure [26, 27]. Then, the as-prepared precursor was carbonized at 600 °C for 5 h under argon atmosphere. During carbonization, the nano-sized $Na_4Ge_9O_{20}$ nanoparticles (through ion-exchanging with NaCl) were uniformly formed inside the carbon framework, leading to the formation of 3D NaCl@$Na_4Ge_9O_{20}$@N-C composites. The prepared 3D NaCl@$Na_4Ge_9O_{20}$@N-C composites were characterized by SEM, XRD and EDS, as shown in Fig. S1. Finally, the remaining NaCl template was washed off by deionized water, leading to the formation of pure 3D $Na_4Ge_9O_{20}$@N-C composites.

The phases and crystal structures of each sample were detected by XRD, as is shown in Fig. 1a. 3D $Na_4Ge_9O_{20}$@N-C, $Na_4Ge_9O_{20}$@N-C, and bare $Na_4Ge_9O_{20}$ exhibit similar patterns (the detailed information of preparation of four samples are shown in Experimental section). All the characteristic peaks can be matched with tetragonal $Na_4Ge_9O_{20}$ (JCPDS No. 73-1587). Specifically, the strong peaks located at 13.4°, 16.7°, 21.5°, 24.6° and 37.9° are indexed to (101), (220), (301), (231) and (620) atomic planes, respectively. The two board peaks around 23° and 44° can be ascribed to (002) and (100) planes of carbon [28], respectively. No other diffraction peaks can be detected, suggesting a high purity of those as-synthesized samples. No obvious carbon peaks are detected in 3D $Na_4Ge_9O_{20}$@N-C composites, which is due to the great crystalline character of $Na_4Ge_9O_{20}$. Therefore, Raman spectra were used to confirm the existence and further explore the structure of carbon.

As shown in Fig. 1b, compared with bare $Na_4Ge_9O_{20}$, carbon-based $Na_4Ge_9O_{20}$ composites and 3D N-C frameworks present two conspicuous bands at 1337.25 and 1573.54 cm^{-1}, which are attributed to D-band (disorder-induced carbon) and G-band (graphitic carbon), respectively [29]. The I_D/I_G ratios of 3D $Na_4Ge_9O_{20}$@N-C, $Na_4Ge_9O_{20}$@N-C and bare $Na_4Ge_9O_{20}$ were calculated to be around 1.09, 1.06 and 1.09, respectively, suggesting the amorphous feature of the N-doped carbon [23, 30].

To figure out the content of carbon within the 3D $Na_4Ge_9O_{20}$@N-C, thermogravimetric analysis (TGA) was performed (Fig. 1c). The sample was heated under air atmosphere from room temperature (25 °C) to 800 °C with a ramping rate of 10 °C·min^{-1}. The slight weight loss below 150 °C could be explained by the removal of adsorbed water. And the following sharp mass loss at

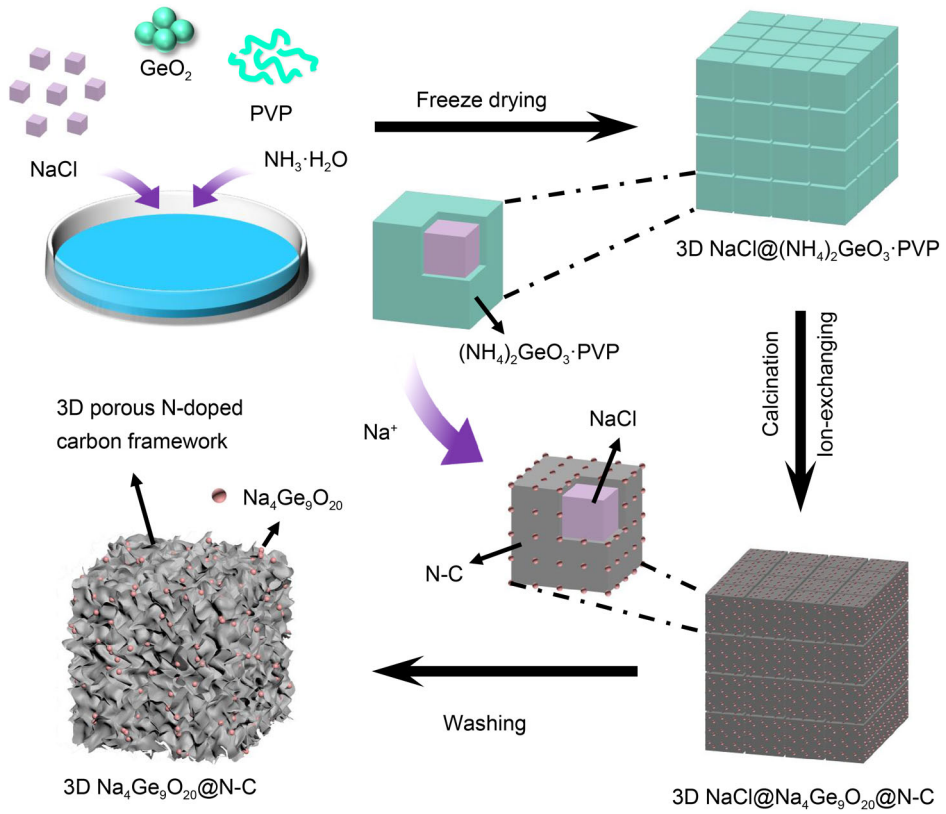

Scheme 1 Schematic illustration of synthetic process of 3D porous interconnected structure of obtained $Na_4Ge_9O_{20}$@N-C composites

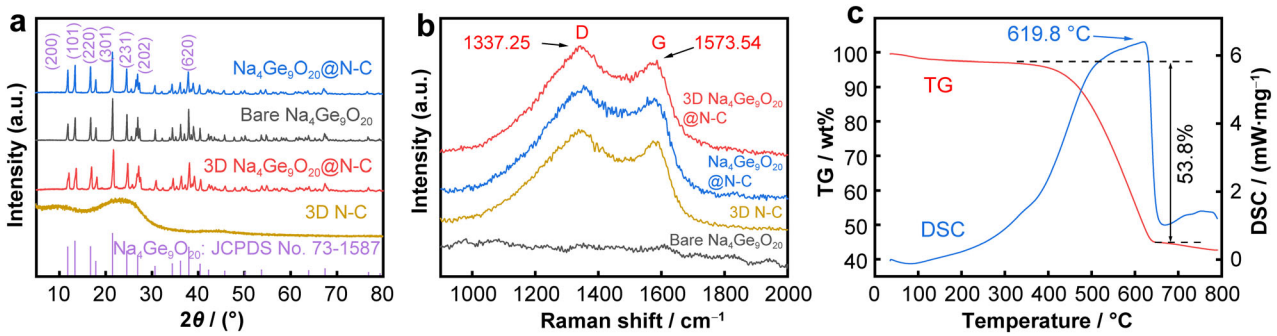

Fig. 1 **a** XRD patterns and **b** Raman spectra of 3D $Na_4Ge_9O_{20}$@N-C, $Na_4Ge_9O_{20}$@N-C, bare $Na_4Ge_9O_{20}$ and 3D N-C; **c** TGA curves of 3D $Na_4Ge_9O_{20}$@N-C in air

around 619.8 °C can be ascribed to the burning of carbon frameworks, indicating that the original content of carbon is calculated to be about 53.8 wt% within the 3D $Na_4Ge_9O_{20}$@N-C composites.

Figure. S1a shows SEM image of the calcined composites before removing NaCl. It can be observed that 3D structure was self-assembled by NaCl particles of different sizes and the salts were embedded in the carbon matrix. As expected, after removing the template, 3D $Na_4Ge_9O_{20}$@N-C possesses a typical 3D interconnected porous structure and displays the highly well-distributed pore (with a diameter of 200–500 nm), as depicted in Fig. 2a. No visible structural collapse is observed. High magnification SEM image (Fig. 2b) of the 3D $Na_4Ge_9O_{20}$@N-C displays a smooth surface of the carbon framework, suggesting that $Na_4Ge_9O_{20}$ particles have been totally wrapped inside the carbon matrix, which can also be further demonstrated from TEM images. SEM–EDS spectra (Fig. S2a) indicate the existence of C, N, O, Na, Ge, Si and the corresponding atomic ratio is also presented (inset in Fig. S2a), which is consistent with the results of XRD. The observation of Si is because the samples were characterized on a silicon wafer.

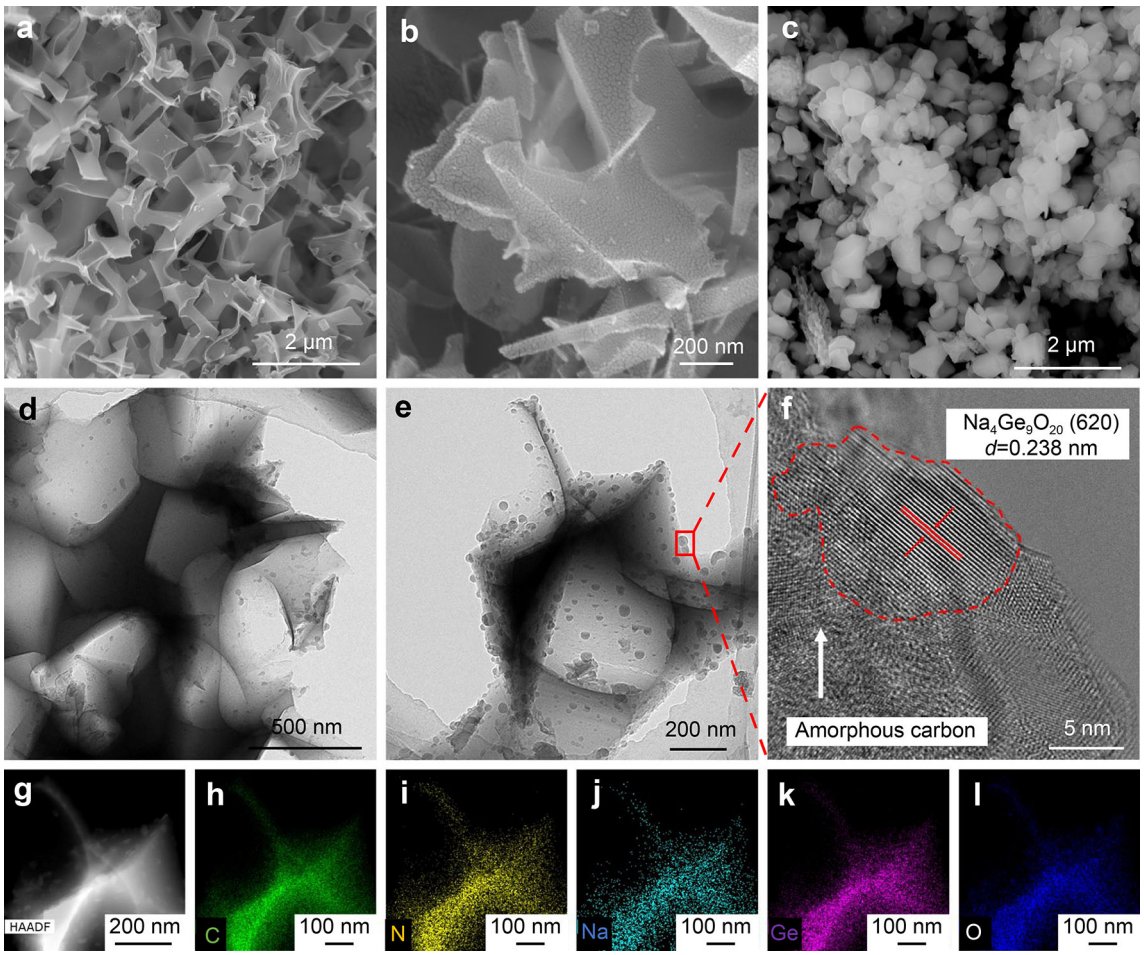

Fig. 2 SEM images of **a, b** 3D $Na_4Ge_9O_{20}$@N-C and **c** bare $Na_4Ge_9O_{20}$; **d, e** TEM images, **f** HRTEM image and **g–l** elemental mapping images of as-prepared 3D $Na_4Ge_9O_{20}$@N-C

The corresponding pore size distribution of all samples was calculated by Brunauer–Emmett–Teller (BET) method. According to Fig. S2b, 3D $Na_4Ge_9O_{20}$@N-C exhibits the largest surface area of 26.8 $m^2 \cdot g^{-1}$, which is higher than that of 3D N-C (24.1 $m^2 \cdot g^{-1}$), $Na_4Ge_9O_{20}$@N-C (14.8 $m^2 \cdot g^{-1}$) and bare $Na_4Ge_9O_{20}$ (8.7 $m^2 \cdot g^{-1}$). Based on Barrett–Joyner–Halenda (BJH) model, the pore size distribution of 3D $Na_4Ge_9O_{20}$@N-C mostly ranges from 2 to 4 nm. The high surface area of 3D porous structures could enlarge the contact area between electrode and electrolyte, and provide more active sites for electrochemical reactions [25]. Besides, compared with 3D $Na_4Ge_9O_{20}$@N-C, 3D N-C shows similar porous structure (Fig. S3a), but $Na_4Ge_9O_{20}$@N-C is composed of $Na_4Ge_9O_{20}$ particles wrapped inside the large carbon blocks (Fig. S3b). Bare $Na_4Ge_9O_{20}$ possesses a typical bulks structure with size of ~ 0.5 μm (Fig. 2c).

Noting that different amounts of GeO_2 added into the synthesis process will greatly affect the morphology of the final materials. As shown in Fig. S4a, when 0.1 g GeO_2 (marked as 3D $Na_4Ge_9O_{20}$@N-C-H) was added, the distinct agglomerations of $Na_4Ge_9O_{20}$ are detected within the carbon matrix, which is unfavorable for the electrochemical performance. When 0.02 g GeO_2 (marked as 3D $Na_4Ge_9O_{20}$@N-C-L) was added, the morphology has a good reservation (Fig. S4b), while the specific capacity is decreased because of the scarcity of $Na_4Ge_9O_{20}$.

TEM image (Fig. 2d) further demonstrates the porous network structure of 3D $Na_4Ge_9O_{20}$@N-C. The creation of pores can be attributed to the dissolution of NaCl particles and the release of gases from the decomposition of PVP during the carbonization. When the magnification was enlarged, the nano-scaled particles were clearly observed inside the carbon matrix (Fig. 2e). The high-resolution TEM (HRTEM) image of the dark part (marked by red lines) depicted in Fig. 2f presents the lattice fringes with a *d*-spacing of 0.238 nm, which is corresponding to (620) plane of $Na_4Ge_9O_{20}$ (JCPDS No. 73-1587). In addition, the amorphous carbon layers around $Na_4Ge_9O_{20}$ particles are detected, which is consistent with the results of Raman

spectra. For comparison, bare $Na_4Ge_9O_{20}$ (Fig. S5a, b) with size of ~ 500 nm shows that the bulks structure with no 3D porous structures are detected, which consisted well with the SEM images discussed above. The elemental mapping results of 3D $Na_4Ge_9O_{20}$@N-C (Fig. 2g–l) confirm that C, O, Na and Ge are homogeneously distributed within the carbon framework, while the homogenous distribution of C and N indicates that the framework is composed of N-doped carbon.

Figure 3 shows XPS analysis of 3D $Na_4Ge_9O_{20}$@N–C. The survey scan spectrum (Fig. 3a) demonstrates the presence of C, N, O, Na and Ge within the composite, which is consistent with the results of EDS. The Na 1s and Ge 3d spectra (Fig. 3b, c) display the strong peaks at the binding energies of 1071.8 and 32.3 eV, indicating that Na and Ge exist in Na^+ and Ge^{4+} oxidation states, respectively [31, 32]. As shown in Fig. 3d, C 1s spectrum can be resolved into three individual peaks, which can be assigned to C–C (284.6 eV), C–O (286.1 eV) and C–N (285.3 eV), respectively [33, 34]. The C–N bonds demonstrate the formation of N-doped carbon again. Furthermore, for N 1s spectrum (Fig. 3e), he three peaks at binding energies of 398.4, 400.0 and 400.8 eV can be indexed to pyridinic-N, pyrrolic-N and graphitic-N, respectively [35, 36]. The pyridinic-N and pyrrolic-N were reported beneficial for facilitating the electronics transportation by producing multiple defects and more active sites, resulting in superior rate capacity [36, 37]. In addition, O 1s spectrum displayed in Fig. 3f can be deconvoluted into two peaks located at around 531.6 and 532.7 eV, corresponding to the Ge–O and C–O, respectively [38, 39].

3.2 Electrochemical Li-ion storage performance and reaction kinetics

The electrochemical performances of the as-obtained composite electrodes were investigated in coin cells. Figure 4a displays the initial three cyclic voltammogram (CV) curves of 3D $Na_4Ge_9O_{20}$@N-C between 0.01 and 3.00 V (vs. Li/Li^+) at a scanning rate of 0.1 $mV{\cdot}S^{-1}$. The crystalline structure of ternary germanium compounds can be regarded as the composites of GeO_2 and metal oxides [13], thus the electrochemical behavior of $Na_4Ge_9O_{20}$ is similar to that of GeO_2. In the first cathodic scan, a sharp peak appeared blow 0.3 V can be assigned to the reduction of the GeO_2 to Ge metal and Li–Ge alloying reaction, accompanied by the solid electrolyte interphase (SEI) formation [4, 32]. For the following cathodic scan, only two obvious reduction peaks are observed at around 0.45 and 0.08 V, indicating the formation of the stable SEI layers. In the anodic scan, two oxidation peaks located at 0.42 and 1.13 V were detected, which are related to the dealloying of the Li–Ge alloys and the reoxidation of Ge, respectively [40, 41]. From the second cycle, the subsequent CV curves are overlapped and no obvious peak shifts are detected, implying high reversibility of 3D $Na_4Ge_9O_{20}$@N-C for

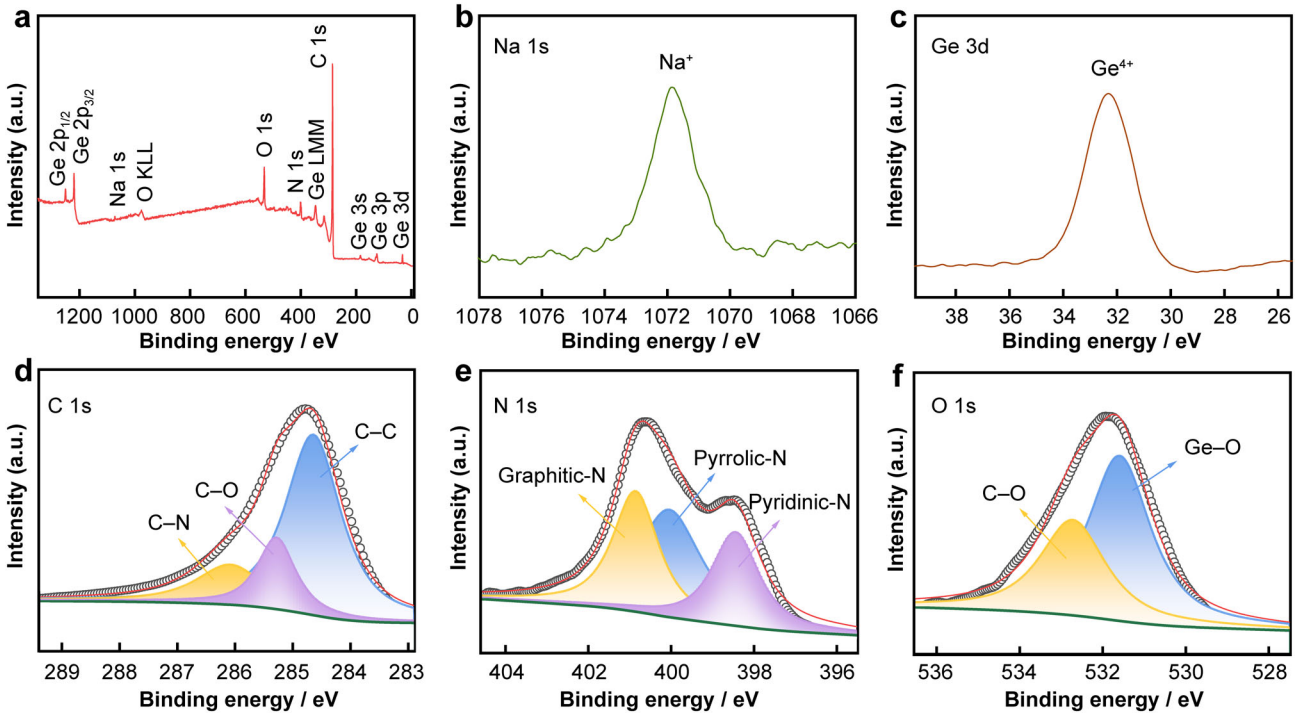

Fig. 3 **a** XPS survey spectrum of 3D $Na_4Ge_9O_{20}$@N-C; high-resolution XPS spectra of **b** Na 1s, **c** Ge 3d, **d** C 1s, **e** N 1s and **f** O 1s of 3D $Na_4Ge_9O_{20}$@N-C composite

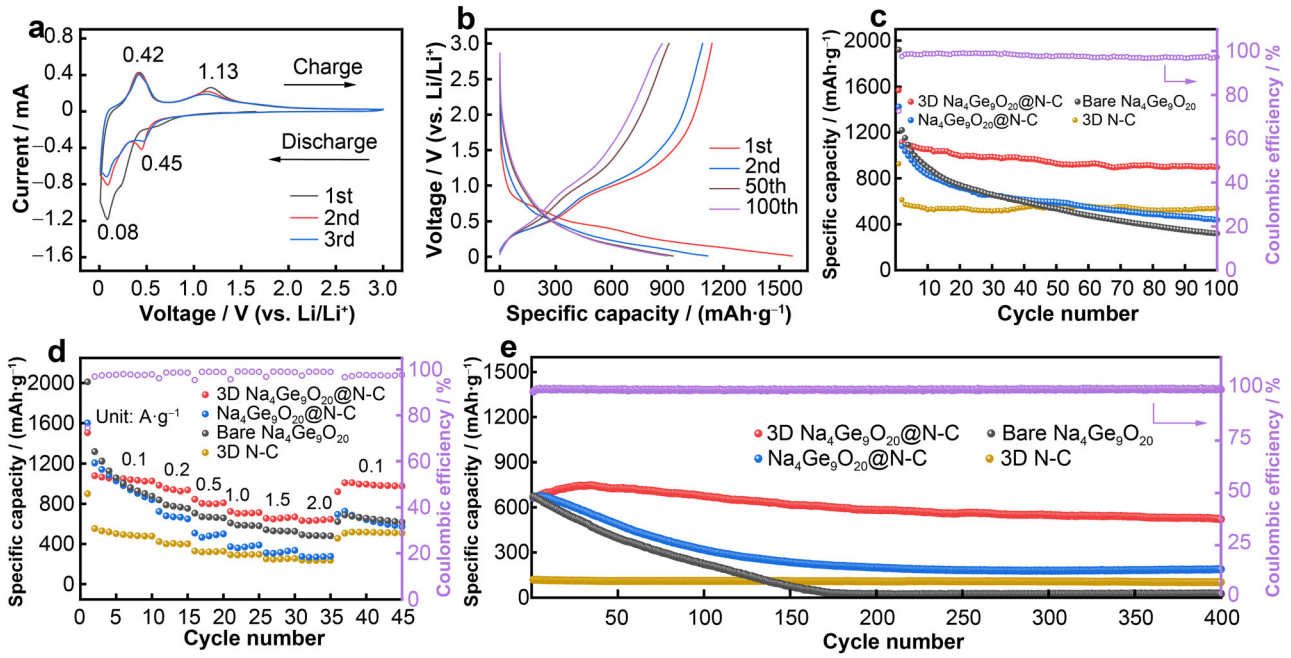

Fig. 4 **a** Initial three successive CV curves of 3D $Na_4Ge_9O_{20}$@N-C at a scan rate of 0.1 mV·s^{-1}; **b** galvanostatic charge/discharge profiles of 3D $Na_4Ge_9O_{20}$@N-C for the 1st, 2nd, 50th and 100th cycles at 0.1 A·g^{-1}; **c** cycling performances at 0.1 A·g^{-1}, **d** rate performances at different current densities from 0.1 to 2.0 A·g^{-1}, and **e** long-term cycling performances at 2.0 A·g^{-1} of 3D $Na_4Ge_9O_{20}$@N-C, $Na_4Ge_9O_{20}$@N-C, bare $Na_4Ge_9O_{20}$ and 3D N-C

lithium storage. The electrochemical reaction mechanism of 3D $Na_4Ge_9O_{20}$@N-C electrode can be described as the following equations [7]:

$$GeO_2 + 4Li^+ \rightarrow Ge + 2Li_2O \quad (1)$$

$$Ge + 4.4Li^+ \leftrightarrow Li_{4.4}Ge \quad (2)$$

Figure 4b presents charge/discharge curves of 3D $Na_4Ge_9O_{20}$@N-C electrode for selected cycles at a current density of 0.1 A·g^{-1}. The voltage plateaus observed in these curves are in well accordance with the redox peaks in CV curves (Fig. 4a). The initial discharge and charge capacities are 1568.6 and 1138.3 mAh·g^{-1}, respectively, corresponding to an initial Coulombic efficiency of 72.6%, which rises to 97.5% in the second cycle and then stabilized thereafter. The irreversible capacity loss of the initial cycle could be attributed to the formation of unstable SEI layer and the decomposition of the electrolyte [21]. The charge/discharge curves are similar from the 50th to the 100th cycle, implying the improved electrochemical reversibility and cycling stability of 3D $Na_4Ge_9O_{20}$@N-C electrode.

Figure 4c compares the cycling performances of 3D $Na_4Ge_9O_{20}$@N-C, $Na_4Ge_9O_{20}$@N-C, bare $Na_4Ge_9O_{20}$ and 3D N-C electrodes at a current density of 0.1 A·g^{-1}. 3D $Na_4Ge_9O_{20}$@N-C electrode apparently exhibits much higher capacity and better stability than $Na_4Ge_9O_{20}$@N-C and bare $Na_4Ge_9O_{20}$. Although bare $Na_4Ge_9O_{20}$ exhibits a high discharge specific capacity of 1220.3 mAh·g^{-1} in the second cycle, only 26.2% of the specific capacity (319.7 mAh·g^{-1}) is retained after 100 cycles, while 3D $Na_4Ge_9O_{20}$@N-C has a capacity retention of 80.4% (896.2 mAh·g^{-1}). This result testifies that the construction of 3D porous interconnected carbon-modified composite could indeed improve the capability of lithium storage and cycling stability, which can be attributed to the enhanced electrical conductivity and its robust structure [7, 36]. Besides, 3D N-C electrode delivers the best cycling stability but the lowest specific capacity (around 530 mAh·g^{-1}) among all samples.

The cycling performances of 3D $Na_4Ge_9O_{20}$@N-C anodes with different contents of $Na_4Ge_9O_{20}$ are also compared in Fig. S6a. Compared with that of 3D $Na_4Ge_9O_{20}$@N-C cycled at current density of 0.1 A·g^{-1}, the capacity of 3D $Na_4Ge_9O_{20}$@N-C-H electrode fades quickly after 5 cycles and retains at only 587.7 mAh·g^{-1} after 50 cycles due to the agglomeration of $Na_4Ge_9O_{20}$ particles. 3D $Na_4Ge_9O_{20}$@N-C-L exhibits excellent cycling stability but much lower capacity (around 590 mAh·g^{-1}), which was just slightly higher than 3D N-C. The condition of cycling performances is similar at a current density of 0.5 A·g^{-1} (Fig. S6b). This result testifies that the content ratio of $Na_4Ge_9O_{20}$ particles and carbon framework in the composites can affect the electrochemical performances. Excessive $Na_4Ge_9O_{20}$ content causes the

agglomeration while less $Na_4Ge_9O_{20}$ content reduces the specific capacity.

Figure 4d shows rate performance of all as-prepared samples. 3D $Na_4Ge_9O_{20}$@N-C delivers the best rate performance with specific capacities of 1035, 948, 811, 710, 658, 636 mAh·g^{-1} at the current densities of 0.1, 0.2, 0.5, 1.0, 1.5, 2.0 A·g^{-1}, respectively. The reversible capacity of 983 mAh·g^{-1} could be recovered when the current density returns to 0.1 A·g^{-1}. In particular, 3D $Na_4Ge_9O_{20}$@N-C maintains a capacity of 636 mAh·g^{-1} at 2.0 A·g^{-1}, which is much higher than those of $Na_4Ge_9O_{20}$@N-C (272 mAh·g^{-1}), bare $Na_4Ge_9O_{20}$ (484 mAh·g^{-1}), and 3D N-C (236 mAh·g^{-1}). $Na_4Ge_9O_{20}$@N-C and bare $Na_4Ge_9O_{20}$ still exhibit rapid capacity decay despite relatively high initial capacity is obtained. As shown in Fig. S6c, among the composites with different contents of $Na_4Ge_9O_{20}$, 3D $Na_4Ge_9O_{20}$@N-C-H exhibits roughly similar rate performance with 3D $Na_4Ge_9O_{20}$@N-C, while 3D $Na_4Ge_9O_{20}$@N-C-L presents a lower rate capability than others, which can be attributed to its too less $Na_4Ge_9O_{20}$ content.

Figure 4e exhibits long-term cycling performances of all the obtained samples at a current density of 2.0 A·g^{-1} after running at 0.1 A·g^{-1} for 5 cycles to stabilize the electrodes. 3D $Na_4Ge_9O_{20}$@N-C shows superior reversible capacity of 520.8 mAh·g^{-1} after 400 cycles with a high Coulombic efficiency of 99.8%, while 3D N-C electrode delivers a low reversible capacity of around 101 mAh·g^{-1}. In sharp contrast, for $Na_4Ge_9O_{20}$@N-C and bare $Na_4Ge_9O_{20}$, only 28.1% (186.6 mAh·g^{-1}) and 3.5% (23.9 mAh·g^{-1}) of the capacity can be maintained after 400 cycles, respectively. By the way, the slightly increase of the capacity of 3D $Na_4Ge_9O_{20}$@N-C at the initial stage may be relevant to the electrochemical activation of electrode material.

Table S1 exhibits the comparison results of our work with previously reported ternary germanium compounds materials. The presented 3D $Na_4Ge_9O_{20}$@N-C anode shows high reversible capacity and competitive rate capability, which demonstrates its promising application for lithium storage. The excellent electrochemical performances of 3D $Na_4Ge_9O_{20}$@N-C in lithium storage can be ascribed to the following reasons: (1) ternary germanium compounds can provide intrinsic high specific capacity; (2) carbon framework derived from PVP can provide buffer layers to suppress the huge volume variation and prevent the direct contact between $Na_4Ge_9O_{20}$ particles and electrolyte; (3) 3D porous structure can provide large specific surface area/void space and short ionic and electronic transport pathway [21, 42]; and (4) the doped nitrogen can further improve the electronic conductivity and provide more storage for lithium ions by producing multiple defects and more active sites [24, 35].

To further study the reaction kinetics of 3D $Na_4Ge_9O_{20}$@N-C electrode, CV measures at different sweeping rates from 0.1 to 2.0 mV·s^{-1} were employed to investigate the lithium storage mechanisms. As shown in Fig. 5a, CV curves exhibit accordant fluctuation at all scan rates. The electrochemical reaction kinetics consist of two typical types: the surface-induced capacitive behavior and the diffusion-controlled faradaic behavior [43]. The capacitance contribution of the reaction can be measured by the following equation [44]:

$$i = av^b \tag{3}$$

where a and b are adjustable parameters calculated by peak current (i) and scan rate (v). Specifically, when the value of b is close to 0.5, the electrochemical kinetics is considered as diffusion-controlled behavior. In contrast, when the value of b is close to 1, the reaction of the system is controlled by the surface capacitive effect [45]. 3D $Na_4Ge_9O_{20}$@N-C shows the b value of 0.59 (Fig. 5b) obtained by the slope of lg$i$-lg$v$ plot for the peak marked in Fig. 5a, indicating that the reaction kinetics of 3D $Na_4Ge_9O_{20}$@N-C are both diffusion reaction and capacitive behavior, but mainly dominated by diffusive behavior.

Moreover, EIS tests were carried out to explore the resistances of 3D $Na_4Ge_9O_{20}$@N-C, $Na_4Ge_9O_{20}$@N-C, bare $Na_4Ge_9O_{20}$ and 3D N-C. As shown in Fig. 5c, all Nyquist plots are composed of a semicircle and an oblique line, which represent the high frequency region and the low frequency region, respectively [46]. The corresponding equivalent circuit model is shown in the inset in Fig. 5c and the primary fitting parameters are listed in Table S2. The charge transfer resistance (R_{ct}) relates to semicircle and the Warburg impedance (Z_w) relates to oblique line. The resistances of the electrolyte, electrode materials and current collectors are represented by R_s. A low R_{ct} value usually indicates low electron transfer resistance. R_{ct} obtained from the equivalent circuit of the 3D $Na_4Ge_9O_{20}$@N-C (151.9 Ω) anode is the minimum compared with those of $Na_4Ge_9O_{20}$@N-C (162.5 Ω), bare $Na_4Ge_9O_{20}$ (190.2 Ω) and 3D N-C (546.9 Ω), indicting the faster electrochemical kinetics of electronic transportation, which can be ascribed to the improved electronic conductivity benefiting from the nitrogen-doped carbon framework.

4 Conclusion

In summary, a 3D porous $Na_4Ge_9O_{20}$@N-doped carbon composite was successfully fabricated via the NaCl-assisted freeze-drying and annealing process. The

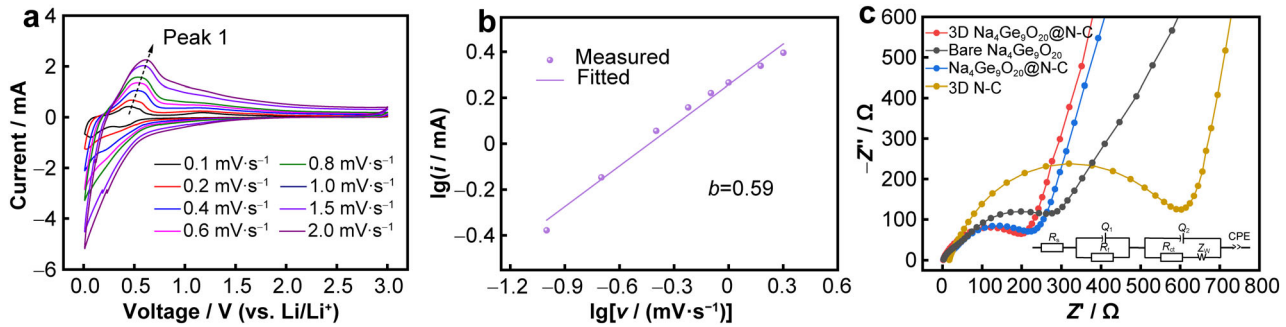

Fig. 5 **a** CV curves of 3D $Na_4Ge_9O_{20}$@N-C at varied scan rates from 0.1 to 2.0 $mV{\cdot}s^{-1}$; **b** corresponding lg*i* versus lg*v* plots (*i* being peak current; *v* being scan rate) at indicated Peak 1; **c** Nyquist plots of 3D $Na_4Ge_9O_{20}$@N-C, $Na_4Ge_9O_{20}$@N-C, bare $Na_4Ge_9O_{20}$ and 3D N-C electrodes and (inset) equivalent circuit for EIS data fitting, where Z' is real part of impedance and Z'' is imaginary part of impedance

microscopic morphologies and electrochemical performances were successfully optimized by adjusting the ratio of $Na_4Ge_9O_{20}$ particles and carbon matrix during the process of preparation. The unique 3D porous N-doped carbon can effectively improve the structural stabilities and cycle performance of the 3D porous $Na_4Ge_9O_{20}$@N-doped carbon composite. Benefiting from the unique structures, when used as anode materials for LIBs, the as-synthesized 3D $Na_4Ge_9O_{20}$@N-C composites exhibit a high capacity of 896.2 $mAh{\cdot}g^{-1}$ after 100 cycles at 0.1 $A{\cdot}g^{-1}$. Even measured at 2.0 $A{\cdot}g^{-1}$, a high capacity of 636.0 $mAh{\cdot}g^{-1}$ can be obtained. The superior electrochemical performances can be ascribed to the N-doped carbon framework. Beside the enhance electronic conductivity toward the $Na_4Ge_9O_{20}$, the employment of the N-doped carbon framework can also improve the electrochemical kinetics, shorten the ionic diffusion distance, and serve as matrix buffers to suppress the huge volume variation of $Na_4Ge_9O_{20}$. This work provides a strategy to improve the electrochemical performance of Ge-based anode materials for lithium-ion batteries.

Acknowledgements This work was financially supported by the National Natural Science Foundation of China (No. 51874362) and the Scientific Research Project of Hunan Provincial Department of Education (No. 21B0815).

Declarations

Conflict of interests The authors declare that they have no conflict of interest.

References

[1] Tarascon JM, Armand M. Issues and challenges facing rechargeable lithium batteries. Nature. 2001;414(6861):359. https://doi.org/10.1038/35104644.

[2] Li XY, Qu JK, Yin HY. Electrolytic alloy-type anodes for metal-ion batteries. Rare Met. 2021;40(2):329. https://doi.org/10.1007/s12598-020-01537-8.

[3] Graetz J, Ahn CC, Yazami R, Fultz B. Nanocrystalline and thin film germanium electrodes with high lithium capacity and high rate capabilities. J Electrochem Soc. 2004;151(5):A698. https://doi.org/10.1149/1.1697412.

[4] Li D, Feng CQ, Liu HK, Guo ZP. Hollow carbon spheres with encapsulated germanium as an anode material for lithium ion batteries. J Mater Chem A. 2015;3(3):978. https://doi.org/10.1039/c4ta05982d.

[5] Bodlaki D, Yamamoto H, Waldeck DH, Borguet E. Ambient stability of chemically passivated germanium interfaces. Surf Sci. 2003;543(1–3):63. https://doi.org/10.1016/s0039-6028(03)00958-0.

[6] Zhang QB, Chen HX, Luo LL, Zhao BT, Luo H, Han X, Wang JW, Wang CM, Yang Y, Zhu T, Liu ML. Harnessing the concurrent reaction dynamics in active Si and Ge to achieve high performance lithium-ion batteries. Energy Environ Sci. 2018;11(3):669. https://doi.org/10.1039/c8ee00239h.

[7] Yan SC, Song HZ, Lin SR, Wu H, Shi Y, Yao J. GeO_2 encapsulated Ge nanostructure with enhanced lithium-storage properties. Adv Funct Mater. 2019;29(8):7. https://doi.org/10.1002/adfm.201807946.

[8] Li CC, Wang B, Chen D, Gan LY, Feng YZ, Zhang YF, Yang Y, Geng HB, Rui XH, Yu Y. Topotactic transformation synthesis of 2D ultrathin GeS_2 nanosheets toward high-rate and high-energy-density sodium-ion half/full batteries. ACS Nano. 2020;14(1):531. https://doi.org/10.1021/acsnano.9b06855.

[9] Lu JX, Li DL, Li L, Chai Y, Li M, Yang S, Liang J. Cobalt-doped Zn_2GeO_4 nanorods assembled into hollow spheres as high-performance anode materials for lithium-ion batteries. J Mater Chem A. 2018;6(14):5926. https://doi.org/10.1039/c8ta00666k.

[10] Li R, Zhang RM, Lou Z, Huang TT, Jiang K, Chen D, Shen GZ. Electrospraying preparation of metal germanate nanospheres for high-performance lithium-ion batteries and room-temperature gas sensors. Nanoscale. 2019;11(25):12116. https://doi.org/10.1039/c9nr03641e.

[11] Liu YW, Zhou TF, Zheng Y, He ZH, Xiao C, Pang WK, Tong W, Zou YM, Pan BC, Guo ZP, Xie Y. Local electric field facilitates high-performance Li-ion batteries. ACS Nano. 2017;11(8):8519. https://doi.org/10.1021/acsnano.7b04617.

[12] Chen Z, Yan Y, Xin S, Li W, Qu J, Guo YG, Song WG. Copper germanate nanowire/reduced graphene oxide anode materials for high energy lithium-ion batteries. J Mater Chem A. 2013;1(37):11404. https://doi.org/10.1039/c3ta12344h.

[13] Li W, Yin YX, Xin S, Song WG, Guo YG. Low-cost and large-scale synthesis of alkaline earth metal germanate nanowires as a new class of lithium ion battery anode material. Energy

Environ Sci. 2012;5(7):8007. https://doi.org/10.1039/c2ee21580b.
[14] Zhou S, Usman I, Wang YJ, Pan AQ. 3D printing for rechargeable lithium metal batteries. Energy Storage Mater. 2021;38:141. https://doi.org/10.1016/j.ensm.2021.02.041.
[15] Lu L, Wang HY, Wang JG, Wang C, Jiang QC. Design and synthesis of ZnO-NiO-Co_3O_4 hybrid nanoflakes as high-performance anode materials for Li-ion batteries. J Mater Chem A. 2017;5(6):2530. https://doi.org/10.1039/c6ta07708k.
[16] Lim YR, Jung CS, Im HS, Park K, Park J, Cho WI, Cha EH. Zn_2GeO_4 and Zn_2SnO_4 nanowires for high-capacity lithium- and sodium-ion batteries. J Mater Chem A. 2016;4(27):10691. https://doi.org/10.1039/c6ta02829b.
[17] Ahmad S, Copic D, George C, De Volder M. Hierarchical assemblies of carbon nanotubes for ultraflexible Li-ion batteries. Adv Mater. 2016;28(31):6705. https://doi.org/10.1002/adma.201600914.
[18] Cha W, Kim IY, Lee JM, Kim S, Ramadass K, Gopalakrishnan K, Premkumar S, Umapathy S, Vinu A. Sulfur-doped mesoporous carbon nitride with an ordered porous structure for sodium-ion batteries. ACS Appl Mater Interfaces. 2019;11(30):27192. https://doi.org/10.1021/acsami.9b07657.
[19] Gou WW, Zhou S, Cao XX, Luo YL, Kong XZ, Chen J, Xie XF, Pan AQ. Agitation drying synthesis of porous carbon supported Li_3VO_4 as advanced anode material for lithium-ion batteries. Rare Met. 2021;40(12):3466. https://doi.org/10.1007/s12598-021-01712-5.
[20] Liu S, Feng J, Bian X, Qian Y, Liu J, Xu H. Nanoporous germanium as high-capacity lithium-ion battery anode. Nano Energy. 2015;13:651. https://doi.org/10.1016/j.nanoen.2015.03.039.
[21] Ngo DT, Le HTT, Kim C, Lee JY, Fisher JG, Kim ID, Park CJ. Mass-scalable synthesis of 3D porous germanium-carbon composite particles as an ultra-high rate anode for lithium ion batteries. Energy Environ Sci. 2015;8(12):3577. https://doi.org/10.1039/c5ee02183a.
[22] Ren XL, Ai DS, Zhan CZ, Lv RT, Kang FY, Huang ZH. NaCl-template-assisted freeze-drying synthesis of 3D porous carbon-encapsulated V_2O_3 for lithium-ion battery anode. Electrochim Acta. 2019;318:730. https://doi.org/10.1016/j.electacta.2019.06.138.
[23] Chen J, Luo YL, Zhang WC, Qiao Y, Cao XX, Xie XF, Zhou HS, Pan AQ, Liang SQ. Tuning interface bridging between $MoSe_2$ and three-dimensional carbon framework by incorporation of MoC intermediate to boost lithium storage capability. Nano-Micro Lett. 2020;12(1):171. https://doi.org/10.1007/s40820-020-00511-4.
[24] Xu HR, Zhao LL, Liu XM, Huang QS, Wang YQ, Hou CX, Hou YY, Wang J, Dang F, Zhang JT. Metal-organic-framework derived core-shell N-doped carbon nanocages embedded with cobalt nanoparticles as high-performance anode materials for lithium-ion batteries. Adv Funct Mater. 2020;30(50):2006188. https://doi.org/10.1002/adfm.202006188.
[25] Sun HT, Mei L, Liang JF, Zhao ZP, Lee C, Fei HL, Ding MN, Lau J, Li MF, Wang C, Xu X, Hao GL, Papandrea B, Shakir I, Dunn B, Huang Y, Duan XF. Three-dimensional holey-graphene/niobia composite architectures for ultrahigh-rate energy storage. Science. 2017;356(6338):599. https://doi.org/10.1126/science.aam5852.
[26] Qin J, He CN, Zhao NQ, Wang ZY, Shi CS, Liu EZ, Li JJ. Graphene networks anchored with Sn@graphene as lithium ion battery anode. ACS Nano. 2014;8(2):1728. https://doi.org/10.1021/nn406105n.
[27] Liu F, Wang YP, Shi JR, Lin JD, Pan AQ. A new strategy to prepare Ge/GeO_2-reduced graphene oxide microcubes for high-performance lithium-ion batteries. Electrochim Acta. 2019;318:314. https://doi.org/10.1016/j.electacta.2019.06.076.
[28] Jafari SM, Khosravi M, Mollazadeh M. Nanoporous hard carbon microspheres as anode active material of lithium ion battery. Electrochim Acta. 2016;203:9. https://doi.org/10.1016/j.electacta.2016.03.028.
[29] Sato K, Saito R, Oyama Y, Jiang J, Cancado LG, Pimenta MA, Jorio A, Samsonidze GG, Dresselhaus G, Dresselhaus MS. D--band raman intensity of graphitic materials as a function of laser energy and crystallite size. Chem Phys Lett. 2006;427(1–3):117. https://doi.org/10.1016/j.cplett.2006.05.107.
[30] Yang YJ, Tang DM, Zhang C, Zhang YH, Liang QF, Chen SM, Weng QH, Zhou M, Xue YM, Liu JW, Wu JH, Cui QH, Lian C, Hou GL, Yuan FL, Bando Y, Golberg D, Wang X. "Protrusions" or "holes'' in graphene: which is the better choice for sodium ion storage? Energy Environ Sci. 2017;10(4):979. https://doi.org/10.1039/c7ee00329c.
[31] Ling MX, Lv ZQ, Li F, Zhao JM, Zhang HM, Hou GJ, Zheng Q, Li XF. Revisiting of tetragonal $NaVPO_4F$: a high energy density cathode for sodium-ion batteries. ACS Appl Mater Interfaces. 2020;12(27):30510. https://doi.org/10.1021/acsami.0c08846.
[32] Yan YH, Liu Y, Zhang YG, Qin CL, Bakenov Z, Wang ZF. Improving the cycling stability of three-dimensional nanoporous Ge anode by embedding Ag nanoparticles for high-performance lithium-ion battery. J Colloid Interface Sci. 2021;592:103. https://doi.org/10.1016/j.jcis.2021.02.026.
[33] Xie XF, Hu Y, Fang GZ, Cao XX, Yin B, Wang YP, Liang SQ, Cao GZ, Pan AQ. Towards a durable high performance anode material for lithium storage: stabilizing N-doped carbon encapsulated FeS nanosheets with amorphous TiO_2. J Mater Chem A. 2019;7(27):16541. https://doi.org/10.1039/c9ta03196k.
[34] Chen J, Pan AQ, Wang YP, Cao XX, Zhang WC, Kong XZ, Su Q, Lin JD, Cao GZ, Liang SQ. Hierarchical mesoporous $MoSe_2$@CoSe/N-doped carbon nanocomposite for sodium ion batteries and hydrogen evolution reaction applications. Energy Storage Mater. 2019;21:97. https://doi.org/10.1016/j.ensm.2018.10.019.
[35] Sun RX, Yue Y, Cheng XF, Zhang K, Jin SY, Liu GY, Fan YX, Bao Y, Liu XD. Ionic liquid-induced ultrathin and uniform N-doped carbon-wrapped T-Nb_2O_5 microsphere anode for high-performance lithium-ion battery. Rare Met. 2021;40(11):3205. https://doi.org/10.1007/s12598-020-01681-1.
[36] Zhang LL, Zhao X, Ji HX, Stoller MD, Lai LF, Murali S, McDonnell S, Cleveger B, Wallace RM, Ruoff RS. Nitrogen doping of graphene and its effect on quantum capacitance, and a new insight on the enhanced capacitance of N-doped carbon. Energy Environ Sci. 2012;5(11):9618. https://doi.org/10.1039/c2ee23442d.
[37] Sang ZY, Zhao ZH, Su D, Miao PS, Zhang FR, Ji HM, Yan X. SiOC nanolayer wrapped 3D interconnected graphene sponge as a high-performance anode for lithium ion batteries. J Mater Chem A. 2018;6(19):9064. https://doi.org/10.1039/c8ta01570h.
[38] Wei HH, Zhang Q, Wang Y, Li YJ, Fan JC, Xu QJ, Min YL. Baby diaper-inspired construction of 3D porous composites for long-term lithium-ion batteries. Adv Funct Mater. 2018;28(3):1704440. https://doi.org/10.1002/adfm.201704440.
[39] Li M, Zhou D, Song WL, Li XG, Fan LZ. Highly stable GeO_x@C core-shell fibrous anodes for improved capacity in lithium-ion batteries. J Mater Chem A. 2015;3(39):19907. https://doi.org/10.1039/c5ta05400a.
[40] Tang W, Liu LL, Zhu YS, Sun H, Wu YP, Zhu K. An aqueous rechargeable lithium battery of excellent rate capability based on a nanocomposite of MoO_3 coated with PPy and $LiMn_2O_4$. Energy Environ Sci. 2012;5(5):6909. https://doi.org/10.1039/c2ee21294c.

[41] Ngo DT, Le HTT, Kalubarme RS, Lee JY, Park CN, Park CJ. Uniform GeO_2 dispersed in nitrogen-doped porous carbon core-shell architecture: an anode material for lithium ion batteries. J Mater Chem A. 2015;3(43):21722. https://doi.org/10.1039/c5ta05145b.

[42] Mo RW, Lei ZY, Rooney D, Sun KN. Three-dimensional double-walled ultrathin graphite tube conductive scaffold with encapsulated germanium nanoparticles as a high-areal-capacity and cycle-stable anode for lithium-ion batteries. ACS Nano. 2019;13(7):7536. https://doi.org/10.1021/acsnano.8b09027.

[43] Li S, Qiu JX, Lai C, Ling M, Zhao HJ, Zhang SQ. Surface capacitive contributions: towards high rate anode materials for sodium ion batteries. Nano Energy. 2015;12:224. https://doi.org/10.1016/j.nanoen.2014.12.032.

[44] Hou BH, Wang YY, Guo JZ, Zhang Y, Ning QL, Yang Y, Li WH, Zhang JP, Wang XL, Wu XL. A scalable strategy to develop advanced anode for sodium-ion batteries: commercial Fe_3O_4-derived Fe_3O_4@FeS with superior full-cell performance. ACS Appl Mater Interfaces. 2018;10(4):3581. https://doi.org/10.1021/acsami.7b16580.

[45] Augustyn V, Come J, Lowe MA, Kim JW, Taberna PL, Tolbert SH, Abruna HD, Simon P, Dunn B. High-rate electrochemical energy storage through Li^+ intercalation pseudocapacitance. Nat Mater. 2013;12(6):518. https://doi.org/10.1038/nmat3601.

[46] Liu XY, Lin N, Xu KL, Han Y, Lu Y, Zhao YY, Zhou JB, Yi Z, Cao CH, Qian YT. Cu_3Ge/Ge@C nanocomposites crosslinked by the in situ formed carbon nanotubes for high-rate lithium storage. Chem Eng J. 2018;352:206. https://doi.org/10.1016/j.cej.2018.07.015.